Instability and Rayleigh conductivity of the jet flow through a circular hole

David Fabre, Paul Bonnefis, Paolo Luchini, and Flavio Giannetti

---

1. Introduction

The problem of an oscillating flow through a circular aperture in a plate is relevant to many applications. (...) One may mention as well the operation of many musical wind instruments.

The case where there is no mean flow has made the object of a number of analytical and numerical investigations. The case of a plate with zero thickness was considered by Rayleigh in the inviscid case. The key result of his solution is that there is a proportionality between the net pressure force felt from both sides of the hole and the acceleration of the fluid, so that the whole situation can be modeled by assuming that there is a rigid plug of fluid, with area πR_h^2 and equivalent length $\ell_{eff} = 2R_h$, oscillating across the aperture. The length ℓ_{eff} was subsequently termed the Rayleigh conductivity, and has been computed for holes of various geometries by (...). This quantity is a key ingredient in the classical modelling of a Helmholtz resonator, whose frequency depends both of the mass of fluid oscillating across the hole and on the compressibility of fluid inside of the cavity. (Ref.)

The effect of viscosity was considered by De Mestre & Guiney in the Stokes limit (...)

Note that in practice nonlinear effects limit the validity of the linearized approach (...)

The case where the flow has a mean component plus a oscillating one, driven for instance by an incoming acoustic field, was considered by Howe. He introduced a key quantity, the Rayleigh conductivity K, which is a complex parameter generalizing the equivalent length ℓ_{eff}. Howe used a jet model, relevant to the large-Reynolds number limit and due to Prandtl and Levi-Civita, which consists of cylindrical shear layer formed at the hole and and forming a *venna contracta*. By considering small-amplitude oscillation of this flow driven by an oscillating upstream pressure, he was able to compute the conductivity as function of the Strouhal number (or dimensionless frequency).

An interesting property of the Rayleigh conductivity is that its real part is directly proportional to the flux of energy transferred from the imposed oscillatory flow to the jet (eq. 4.6 of Howe). In the calculation of Howe, this imaginary part was always positive, meaning that the jet acts as a sink of energy. The situation where this imaginary part is negative, not envisaged by Howe, would mean that the jet is a possible, indicating the possibility for spontaneous oscillations. Thus, the Rayleigh conductivity is actually a useful concept to detect a possible instability.

In the absence of an external unsteady forcing, a jet formed through a hole in a plate can effectively lead to spontaneous oscillations. Such oscillation manifest by the emission of strong whistling tones. This property was already identified by Bouasse who remarked
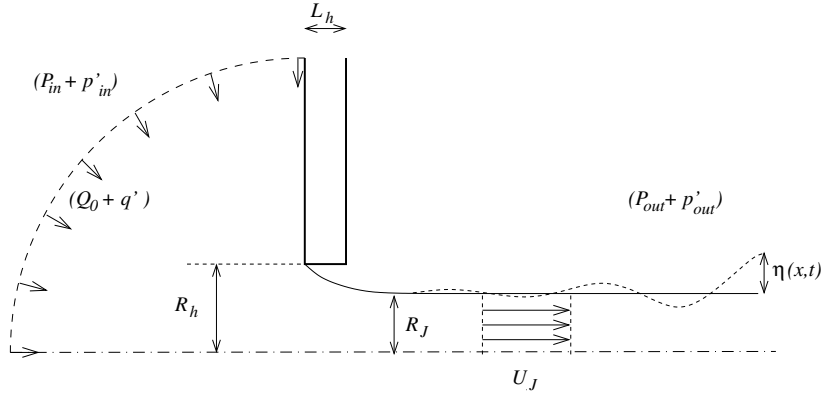
FIGURE 1. Oscillating flow through a circular hole : inviscid modeling

that the frequency of the tone is proportional to the thickness of the hole. (Recent litterature on this ??) The instability mechanism seems to be related to the existence of a recirculation flow inside the hole. Note that the existence of a recirculation region is a necessary condition for global instability in a number of situations, including wakes of bluff bodies and cavity flows (Refs). Yet the conditions of existence of such a recirculation region, and its relationship with instability, remains to be clarified.

The objectives of the present paper can be summarized in three main points. First, we wish to design a numerical approach to compute the steady and insteady flow through a circular aperture for a viscous jet with arbitrary Reynolds number. The problem is notoriously difficult for two reasons. First, the base flow is characterized by a shear layer which remains very steep far away from the aperture, leading to the necessity of a very long computational domain in the axial direction. Secondly, the jet is strongly convectively unstable due to the Kelvin-Helmholtz instability, and it is difficult to design a method capturing both the coupling between the flow rate and the pressure jump, which is relevant when considering the possible coupling with an acoustical system, and the spatial growth of perturbations in the axial direction, which can reach huge levels when the axial distance and the Reynolds number are large. We will introduce an original method, based on a change of variable of the axial coordinate x in the complex plane, which allows to perform accurate computations up to $Re = 10^4$.

Secondly, we will reconsider the case of a hole of zero thickness. We document the base flow and the conductivity for Reynolds number in the range $10^2 - 10^4$ and compare with the predictions of Howe based on an inviscid model.

Thirdly, we apply the approach to a hole of nonzero thickness. We first detect the possibility of instability by computing the imaginary part of Rayleigh conductivity, and show that this quantity effectively becomes negative when there is a recirculation region of sufficient intensity. We finally demonstrate the relationship between the Rayleigh conductivity and the instability by performing a global stability analysis.

2. Problem definition and review of inviscid models

2.1. *Problem definition*

The situation considered here is the flow of an incompressible fluid of density ρ and viscosity ν through a circular hole or radius R_{hole} and area $S_{hole} = \pi R_{hole}^2$ inside a planar plate of thickness H_{hole}, connecting an inner domain and an outer domain. We note Q the volumic flux through the hole, defined as follows :

$$Q = \int_{\mathcal{S}} \mathbf{u} \cdot \mathbf{n} dS,$$

where $\mathcal{S}$ is any surface traversed by the flow, and $\mathbf{n}$ the normal vector at this surface.

We also note p_{in} and p_{out} the pressure levels far away from the hole, in the upstream and downstream domain respectively.

2.2. *Steady flow*

Consider, first, the steady flow. We note Q_0, P_{in} and P_{out} the values of the volumic flux, upstream and downstream pressure.

In the inviscid case, a classical model was proposed by Levi-Civita and Prandtl. The model consists of a vortex sheet formed at the hole, surrounding the jet (see figure 1). After several diameters, the jet becomes parallel, but with a radius R_J smaller than that of the hole. We classically call the ratio of surfaces $\alpha = (\pi R_J^2)/(\pi R_h)$ The *venna contracta* coefficient. This coefficient is classically associated to the pressure loss across the aperture. Assuming a constant velocity U_J inside the jet, the conservation of flux through the hole leads to $Q = \pi R_J^2 U_J = \pi R_h^2 U_M^2$. Applying the Bernoulli theorem along streamlines passing through the hole thus leads to

$$[P_{in} - P_{out}] = \frac{\rho U_J^2}{2} = \frac{\alpha^2 \rho U_M^2}{2}$$

Theoretical calculations by Prandtl and Levi Civita provide the value $\alpha = 0.5$ while experiments indicate typical values in the range $0.61 < \alpha < 6.64$ for Large-Reynolds number flows. The global approach used in the sequel will allow to compute rigorously this parameter for arbitrary values of the Reynolds number, assuming laminar flow.

2.3. *Unsteady flow*

We now reconsider the relationship between the pressure jump and the flow rate in the unsteady case, assuming a harmonic time dependance with frequency ω. Hence, upstream and downstream pressure levels and the flow rate are

$$p_{in} = P_{in} + p_{in}' e^{-i\omega t}; \quad p_{out} = P_{out} + p_{out}' e^{-i\omega t}; \quad Q = Q_0 + q' e^{-i\omega t}.$$

It is convenient to introduce the Strouhal number Ω

$$\Omega = \frac{\omega R}{U_M}.$$

We are still interested in the relationship between pressure jump and flow rate. This relationship can be characterized by the *impedance* of the hole, defined as

$$Z = \frac{[p_{in}' - p_{out}']}{q'}.$$

An alternative definition was introduced by Rayleigh, who defined the *conductivity* K of the aperture as follows :

$$K = \frac{-i\omega\rho q'}{[p'_{in} - p'_{out}]}.$$

The advantage of this definition is that it has the physical dimension of a length, and a simple physical interpretation. Namely, one can recognize in this definition a proportionality between the acceleration of the fluid through the aperture and the net force exerted on it. Indeed, this proportionality can be recovered by assuming that the fluid in the vicinity of the hole behaves as a simple solid plug with mass $\rho\pi R_h^2 K$ oscillating across the hole. Hence, when it is real, K can be interpreted as the *equivalent lengh* of fluid, a quantity which appears, for instance, in the classical modeling of the Helmholtz resonator. For a hole of zero thickness, Rayleigh gives the theoretical value $K = 2R$, while for a very thick plate ($L_h \gg R_h$) one has $K = L_h + 1.28R_h$ (to be checked, and give references).

The problem of Rayleigh was reconsidered by Howe, in presence of a base flow, leading to a prediction for the conductivity as function of the Strouhal number. The derivation is extremely technical and not reproduced here. The final result amounts to :

$$K = 2R(\Gamma - i\Delta)$$

with

$$\Gamma = \frac{I_1(\Omega^*)^2[1 + 1/\Omega^*] + (4/\pi^2)e^{2\Omega^*}\cosh(\Omega^*)K_1(\Omega^*)^2[\cosh(\Omega^*) - \sinh(\Omega^*)/\Omega^*]}{I_1(\Omega^*)^2 + (4/\pi^2)e^{2\Omega^*}\cosh^2(\Omega^*)K_1(\Omega^*)^2}$$

$$\Delta = \frac{(2/\pi\Omega^*)I_1(\Omega^*)K_1(\Omega^*)e^{2\Omega^*}}{I_1(\Omega^*)^2 + (4/\pi^2)e^{2\Omega^*}\cosh^2(\Omega^*)K_1(\Omega^*)^2}$$

Note that in the calculation of Howe, the Strouhal number is defined as $\Omega^* = \omega R/U$ where U is the velocity of convection of the vorticity along the vortex sheet. Howe argues that $U = U_J/2$, in accordance with classical modeling of the Kelvin-Helmholtz instability. Hence the relationship with the Strouhal number used in the present paper is $\Omega^* = \Omega/(2\alpha)$, and the two definitions are equivalent if $\alpha = 1/2$.

3. The viscous problem : analysis and numerical method

3.1. *Parameters and general equations*

The dimensions of the inner and outer domains are assumed to be large compared to the dimensions of the hole, so the only physically meaningful parameter is the aspect ratio of the hole defined as follows :

$$\beta = \frac{L_{hole}}{R_{hole}}.$$

Taking the diameter $2R_{hole}$ as a length scale and the average velocity through the hole $U_M/\pi R_{hole}^2$ as a velocity scale, we can define a Reynolds number and an aspect ratio :

$$Re = \frac{2R_{hole}U_M}{\nu} \equiv \frac{2Q}{\pi R_{hole}\nu};$$

The problem is governed by the Navier-Stokes equations which are written in the following form

$$\frac{\partial}{\partial t} \left[\begin{array}{c} \mathbf{u} \\ 0 \end{array} \right] = \mathcal{NS} \left[\begin{array}{c} \mathbf{u} \\ p \end{array} \right] = \left[\begin{array}{c} -\mathbf{u} \cdot \nabla \mathbf{u} - \nabla p + \nu \Delta \mathbf{u} \\ \nabla \cdot \mathbf{u} \end{array} \right] \tag{3.1}$$

The flow is further decomposed into a base flow $[\mathbf{u_0}; p]$ associated with the mean flux Q_0 and a small-amplitude perturbation $[\mathbf{u}'; p']e^{-i\omega t}$ associated with the oscillating flux $q'e^{-i\omega t}$. The base flow obeys the steady Navier-Stokes equations $\mathcal{NS}[\mathbf{u_0}; p] = 0$ and the perturbations obeys the linear equation $-i\omega[\mathbf{u}'; 0] = \mathcal{L}_0[\mathbf{u}'; p']$ where $\mathcal{L}_0$ is the linearized Navier-Stokes operator about the base flow, defined as follows:

$$\mathcal{L}_0 \left[\begin{array}{c} \mathbf{u}' \\ p' \end{array} \right] = \left[\begin{array}{c} -(\mathbf{u}_0 \cdot \nabla \mathbf{u}' + \mathbf{u}' \cdot \nabla \mathbf{u}_0) - \nabla p' + \nu \Delta \mathbf{u}' \\ \nabla \cdot \mathbf{u}' \end{array} \right] \tag{3.2}$$

The detailed expression of these operators will be given below. The flow obviously verifies no-slip conditions $\mathbf{u} = \mathbf{0}$ on the wall (noted Γ_w), and symmetry conditions at the axis (noted Γ_{ax}). The treatment of the geometry and boundary conditions in the upstream and downstream domain require special attention and are detailed bellow.

3.2. *Upstream domain*

As sketched in figure 1, the upstream domain is expected to originate from an upstream container of large dimension, and sufficiently far away from the hole the flow is assumed to be radially convergent. However, in the numerical implementation, it is required to specify a given geometry for this upstream domain. Here, we have chosen to assume that the upstream region is a closed cavity of rectangular cross-section, with radius R_{cav} and length L_{cav}. The volumic flux condition is imposed by assuming that both the base-flow and the perturbation velocities are constant along the bottom of the cavity, noted Γ_{in}

$$\mathbf{u}_0 = -Q_0/S_{cav}\vec{n}; \quad \mathbf{u}' = -q'/S_{cav}\vec{n} \quad \text{at} \Gamma_{in} \tag{3.3}$$

where $S_{cav} = \pi R_{cav}^2$ is the area of the bottom wall and $\mathbf{n}$ is the outward normal vector. The pressure levels P_{in} and p'_{in}, which are required for the calculation of the mean pressure loss and the conductivity, are computed by averaging along the inlet boundary :

$$P_{in} = 1/S_{cav} \int_{\Gamma_{in}} P_0 2\pi r dr; \quad p'_{in} = 1/S_{cav} \int_{\Gamma_{in}} p' 2\pi r dr. \tag{3.4}$$

It was verified that if the dimensions of the cavity are large enough, the pressure is effectively nearly constant along the inlet boundary Γ_{in}.

At the lateral wall of the cavity, noted Γ_{lat}, the physically relevant condition should be a no-slip condition. However, as the location of this wall is not really relevant, and in order to avoid the development of a boundary layer, we preferred to impose a stress-free condition, namely

$$\mathbf{u} \cdot \mathbf{n} = 0; \quad \frac{\partial(\mathbf{u} \cdot \mathbf{x})}{\partial r} = 0 \quad \text{at } \Gamma_{lat}, \tag{3.5}$$

which applies for both the base flow and the perturbation.

In the sequel we set the dimensions of the upstream cavity as $L_{cav} = R_{cav} = 10R_{hole}$, and verified that these values are large enough for the results to be insensible to these parameters.

3.3. *Downstream domain : boundary conditions and change of coordinates*

The treatment of the outlet conditions is a delicate point here, as the structure of both the base flow and the perturbation lead to some difficulties, especially when the Reynolds number becomes large. These difficulties led us to use an original method which consists of

using a change of variables from a computational domain defined with $[X, R]$ coordinates to the physical domain with $[x, r]$ coordinates.

The first motivation for this method comes from the structure of the base flow. In effect, the laminar, steady solution $[u_0, p_0]$ is characterized by a boundary layer which remains very sharp at large distances from the hole. More specifically, the boundary layer thickness δ scales as $\delta(x) \approx \sqrt{\nu x / U_J} \approx Re^{-1/2} x^{1/2}$. Of course, in a real, High-Reynolds jet, the boundary layer thickness grows much faster because of turbulence. However, the global method used here requires computation of a laminar base flow so we have to work around this issue. The solution is to use a change of coordinates $x = G_x(X)$ which stretches the outer domain from $X \in [0, X_{max}]$ to $[0, x_{max}]$, where the bound of the computational X_{max} is relatively small, while the corresponding $x_{max} = x(X_{max})$ is several orders of magnitude larger.

The second issue is due to the structure of the perturbation. In effect, the jet is spatially unstable, and thus perturbations are convectively amplified in the downstream perturbation, and far away from the hole, they reach levels several orders of magnitude larger than the levels in the vicinity of the hole. As soon as the ratio between minimum and maximum levels of the perturbation becomes of the order of the numerical round-off error (10^{-15} using double-precision) this issue leads to the impossibility to compute accurately the structure of the perturbation in the vicinity of the whole, which is mostly relevant for the computation of the conductivity. In practice, when solving the problem in terms of the physical coordinates, this issue limits the validity of the results to $Re \leqslant 800$.

To detail the origin of the problem and introduce the idea used to overcome it, let us review the classical modeling of the Kelvin-Helmholtz instability for a planar shear layer of zero thickness in the inviscid case. The derivation can be found in any classical textbook on hydrodynamical stability (e.g. Shandrasekar, Drazin & Reid, Charru, etc..). Consider as a base flow a shear layer separating two regions of constant axial velocity, namely $u = U$ for $y < 0$ and $u = 0$ for $y > 0$. Now assume that the perturbation consists of a displacement of the shear layer with the form

$$y = \eta \approx e^{ikx - i\omega t} \tag{3.6}$$

and assume a similar modal expansion for the velocity potential in the upper and lower region. Matching the two regions at the interface leads to the classical dispersion relation :

$$c \equiv \frac{\omega}{k} = \frac{1 + i}{2} U \tag{3.7}$$

In a temporal stability framework, this means that a perturbation with real wavenumber k will be convected downstream with a phase velocity $U/2$ and temporally amplified with a growth rate $Uk/2$. On the other hand, in a spatial stability framework (ω real, k complex), which is more relevant here, this means that any perturbation will be spatially amplified downstream and will diverge at $x \to +\infty$. This divergence forbids a global resolution of the function $\eta(x, t)$ when the spatial variable x is *real*. However, the problem disappears if we consider an analytical continuation of the function $\eta(x, t)$ with a *complex variable x*. More specifically, as $\arg(k) = -\pi/4$, the function $\eta(x, t)$ becomes convergent as soon as $|x| \to \infty$ in a direction of the complex plane verifying $\pi/4 < \arg(x) 5\pi/4$.

Thus, this study of the simple, inviscid, planar shear layer suggests a possible way to resolve the problem for the present case of a viscous, cylindrical shear layer : using a *complex coordinate change* which maps the numerical $X \in [0; X_{max}]$ (with X real) into a path for the physical x coordinate which enters the complex plane and follows a direction where the perturbation is spatially damped.

Combining both ideas, namely stretching and complex deformation, we have used the following mapping function from numerical coordinate X to physical coordinate x :

$$
\begin{aligned}
x = G_x(X) &= \frac{x}{[1-X^2/L_s^2]^2}\left[1 + i\gamma_c \tanh\left(\frac{X}{L_c}\right)^2\right] &\text{for } X > 0, \\
&= x &\text{for } X < 0.
\end{aligned}
\tag{3.8}
$$

This choice has the following properties. First, it leaves the axial coordinate unchanged in the upstream domain and inside the hole ($x < 0$). Secondly, the numerical and spatial coordinates are also almost identical in the region where the jet emerges from the hole (namely $x \leqslant L_c$ and $x \leqslant L_s$). Thirdly, as X approaches the upper bound of the numerical domain X_{max}, and complex, the physical variable tends to $x_{max} = G_x(X_{max}$, which is very large as soon as L_c is close to X_{max} (with $L_s > X_{max}$), and complex, with argument $\tan^{-1}(\gamma_c)$, as soon as $\gamma_c \neq 0$.

Finally, although the issue is less crucial for the axial coordinate, we also used a change of coordinates $R(r)$ to stretch the radial coordinate from $R \in [0, R_{max}]$ to $r \in [0, r_{max}]$. Here there is no point in using a complex deformation, so we used the following mapping function :

$$
\begin{aligned}
r = G_r(R) &= R_{s1} + \frac{R - R_{s1}}{[1 - (R - R_{s1})^2/(R_{s2} - R_{s1})^2]^2} &\text{for } X > 0 \text{ and } R > R_{s1}, \\
&= r &\text{otherwise}
\end{aligned}
\tag{3.9}
$$

This function leaves the radial coordinate unchanged in the upstream domain an in the region $r < R_{s1}$ where the jet develops, but it stretches the limit of the domain from R_{max} to $r_{max} = G_r(R_{max})$ which is very large as soon as R_{s2} is close to R_{max} (with $r_{s2} > R_{max}$).

Having explained this change of coordinates, it remains to specify the boundary conditions to be used at the outer limits of the computational domain. For the resolution of the Navier-Stokes equation in an open domain, the physically relevant boundary condition $[\mathbf{u}; p] \to [0; p_{out}]$ as $(x, r) \to \infty$ are often replaced by setting the traction (or pseudo-stress) $-p\mathbf{n} + \nu\nabla\mathbf{u} \cdot \mathbf{n}$ to zero at the outlet boundaries. An alternative choice is to nullify the stress $-p\mathbf{n} + \nu(\nabla\mathbf{u} + \nabla\mathbf{u}^T) \cdot \mathbf{n}$. In the present case, we have chosen to impose a zero-traction condition at the boundaries x_{max}, r_{max}, for both the base flow and the perturbation. A zero-stress condition was also tried, leading to similar results but convergence difficulties when computing the base flow. Note that the significance of

Note that the use of complex coordinate mapping for linear problems involving a single spatial coordinate is customary in stability studies, and mathematical theorems are available to justify how to chose the integration contour as function of the singularities of the problem (e.g. Bender & Orzag). On the other hand, its use for a nonlinear problem (i.e. computation of the base flow) involving two spatial coordinates is totally new to our knowledge. The validity of the method is not justified by rigourous mathematical argument, but only by the fact that it effectively works and that the results are independent upon the parameters of the mapping. A few test showing that it is effectively the case, for both the base flow and the perturbation, are given in appendix A.

For most results presented in the present paper, the following choice of parameters was used:

$$
R_{cav} = L_{cav} = 10; R_{max} = X_{max} = 15; X_s = 16; X_c = 2.5; \gamma_c = 0.3; R_{s1} = 5; R_{s2} = 16.
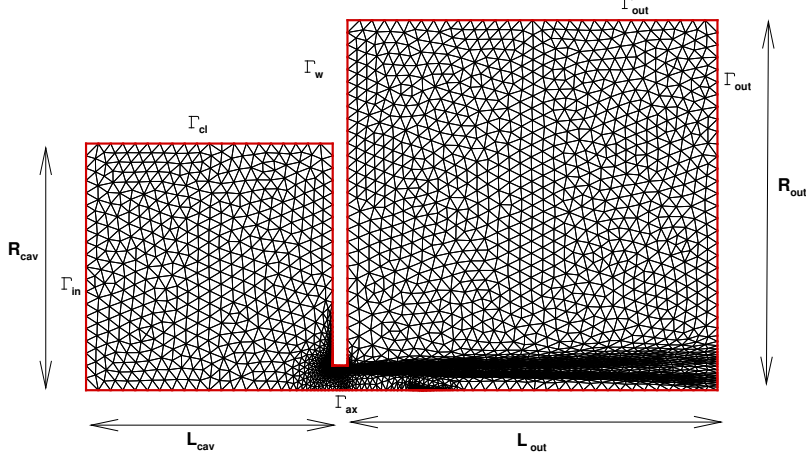$$

FIGURE 2. Example of computational mesh with dimensions in mapped coordinates and nomenclature of boundaries.

In terms of the physical coordinates, this means that the outer boundaries are located at $x_{max} = 1022 + 306i; r_{max} = 337$.

3.4. *Numerical implementation*

The numerical resolution of the problem was performed with a finite element method, using the FreeFem++ software. An example of computational mesh, in the $[X, R]$ coordinates, is shown in figure 2. Meshes were generated using Delaunay-Voronoi triangulation of the domain, and subsequently refined locally to fit the steep gradients of both the base flow and the perturbation using the adaptmesh command provided by the Freefem++ software.

For resolution, the Navier-Stokes equations have first to be expressed in terms of the mapped coordinates. For this purpose, the spatial derivatives have to be modified as follows :

$$\frac{\partial}{\partial x} \equiv H_x \frac{\partial}{\partial X} \quad \text{with } H_x = \frac{1}{G'_x}; \tag{3.10}$$

$$\frac{\partial}{\partial r} \equiv H_r \frac{\partial}{\partial R} \quad \text{with } H_r = \frac{1}{G'_r}. \tag{3.11}$$

The incompressible Navier-Stokes operator thus have the following form :

$$\mathcal{NS} \begin{bmatrix} u_x \\ u_r \\ p \end{bmatrix} = \begin{bmatrix} -(u_x H_x \partial_X u_x + u_r H_r \partial_R u_x) - H_x \partial_X p + \nu \left[H_x \partial_X (H_x \partial_X u_x) + H_r/r \partial_R (r H_r \partial_r u_x) \right] \\ -(u_x H_x \partial_X u_r + u_r H_r \partial_R u_r) - H_r \partial_R p + \nu \left[H_x \partial_X (H_x \partial_X u_r) - u_r/r^2 + H_r/r \partial_R (r H_r \partial_r u_r) \right] \\ H_x \partial_X u_x + H_r/r \partial_R (r u_r) \end{bmatrix} \tag{3.12}$$

to solve these equations using finite element method, we classically multiply by test functions $[u_x^*, u_r^*, p^*]$ and integrate over the domain. Note that this integration has to be done over the physical domain, so in terms of the numerical variables the elementary volume of integration is $dV = rdrdx = (H_x H_r)^{-1} rdRdX$. After integration by parts

of the pressure gradient and Laplacian terms, we are thus lead to the following weak formulation:

$$
\begin{aligned}
&-\int \left[u_x^* \left(u_x H_x \partial_X u_x + u_r H_r \partial_R u_x \right) + u_r^* \left(u_x H_x \partial_X u_r + u_r H_r \partial_R u_r \right) \right] dV \\
&+\int \left[p \left(H_x \partial_X u_x^* + H_r \partial_R u_r^* + u_r^*/r \right) - p^* \left(H_x \partial_X u_x + H_r \partial_R u_r + u_r/r \right) \right] dV \\
&-\int \left[H_x^2 \partial_X u_x \partial_X u_x^* + H_r^2 \partial_R u_x \partial_R u_x^* \right] dV \\
&-\int \left[H_x^2 \partial_X u_r \partial_X u_r^* + H_r^2 \partial_R u_r \partial_R u_r^* + u_r u_r^*/r^2 \right] dV \\
&= 0.
\end{aligned}
\tag{3.13}
$$

Note that with this formulation, the no-traction boundary conditions at the outlet boundary, as well as the symmetry condition at the axis and the zero tangential stress condition at the lateral wall of the cavity are automatically satisfied thanks to the integration by parts. The other boundary conditions are imposed by penalization.

Following a now customary approach, the computation of the base flow is done using a standart Newton. The algorithm is as follows :

(i)Start from a guess flow field $[\mathbf{u}^g; p^g]$.

(ii)Solve the linear system $\mathcal{NS}[\mathbf{u}^g, p^g] + \mathcal{L}_g[\delta\mathbf{u}, \delta p]$ where $\mathcal{L}_g$ is the linearized Navier-Stokes operator around the guess field.

(iii)Obtain a better guess as $[\mathbf{u}, p] = [\mathbf{u}^g, p^g] + [\delta\mathbf{u}, \delta p]$.

(iv)Repeat until convergence.

The inversion at step (ii) is done with the UMFPACK64 library.

In practice, at point (i) the guess field is generally taken as the base flow computed at a lower value of the Reynolds number. The whole algorithm is thus repeated for increasing values of the Reynolds number to generate a family of base flow. The mesh refinement is applied at each step, so that the refinement, and the number of points of the mesh, increases with the Reynolds number. Note that when using the complex mapping method described above, the radius of convergence of the Newton algorithm seems to be smaller than in the standard case. This means that the Reynolds number has to be increased moderately between successive base flow computations.

The computation of the perturbations due to harmonic forcing $[u_x', u_r', p']$ is done using the same linear solver UMFPACK64. Note that the structure may involve steeper gradients compared to the base flow. To capture this, the problem is first solved on the refined mesh computed during the base flow computation. The mesh is subsequently refined a second time through the adaptmesh command, and the base flow and the perturbation are finally recomputed on this better mesh.

4. The zero-thickness case

Validations and illustration of the efficiency of the complex mapping method.

4.1. *Steady base flow*

4.2. *Unsteady flow*

Illustration of the structures, with and without complex coordinate mapping.
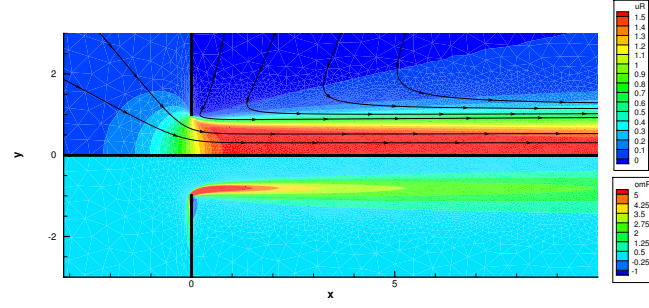
Rayleigh conductivity, comparison with Howe.

FIGURE 3. Base flow for $Re = 500, L_h = 0$ (in physical coordinates (x, r), without mapping). Upper part : axial velocity u_{x0} and streamlines. Lower part : vorticity.
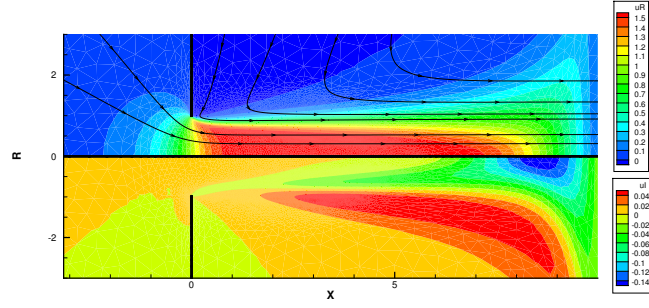

FIGURE 4. Base flow for $Re = 500, L_h = 0$ (in numerical coordinates (X, R), with complex mapping). Upper part : $Re(u_{x0})$ and pseudo-streamlines. Lower part : $Im(u_{x0})$
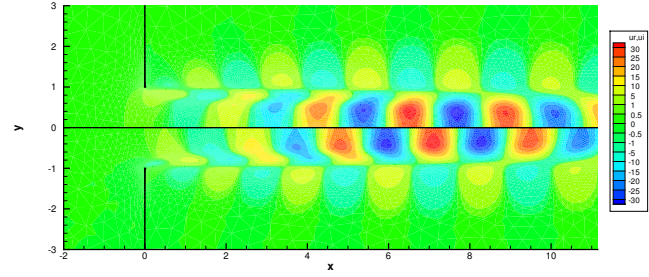

FIGURE 5. Harmonic perturbation for $Re = 500, \Omega = 3$ (in physical coordinates (x, r), without mapping). Real (upper) and imaginary (lower) parts of the axial velocity component u'.
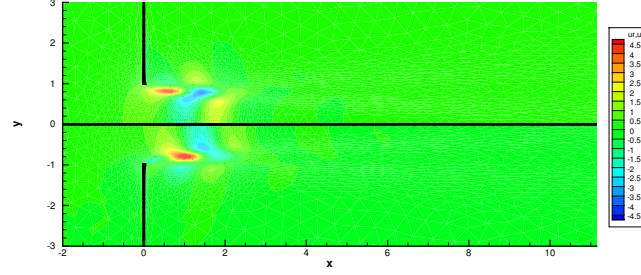
FIGURE 6. Harmonic perturbation for $Re = 500, \Omega = 3$ (in numerical coordinates (X, R), with complex mapping). Real (upper) and imaginary (lower) parts of the axial velocity component u'.
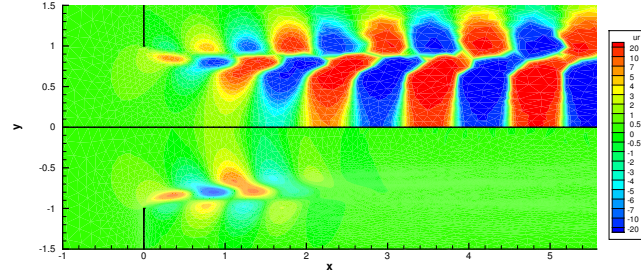

FIGURE 7. Harmonic perturbation for $Re = 1000, \Omega = 5$. Real part of the pressure component. Upper part : in physical coordinates (x, r) ; lower part : in numerical coordinates (X, R), with complex mapping. Real (upper) and imaginary (lower) parts of the axial velocity component u'.
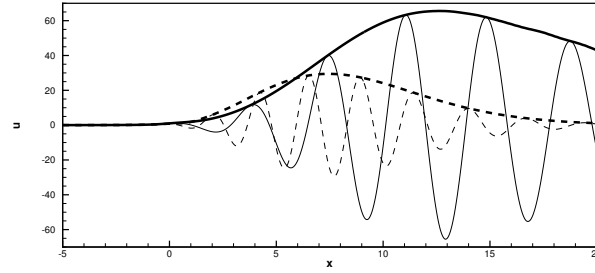
FIGURE 8. Axial velocity (real part ; modulus) along the symmetry axis for $Re = 500$ and $\Omega = 2$ (plain lines) and $\Omega = 3$ (dashed lines).
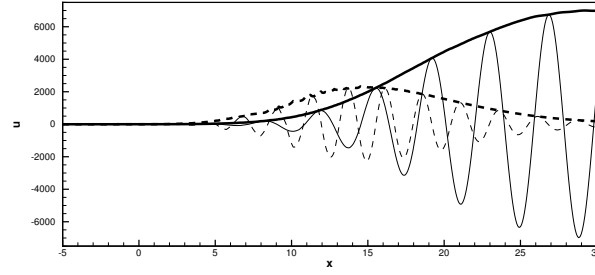
FIGURE 9. Same as in figure 8 but for $Re = 1000$.
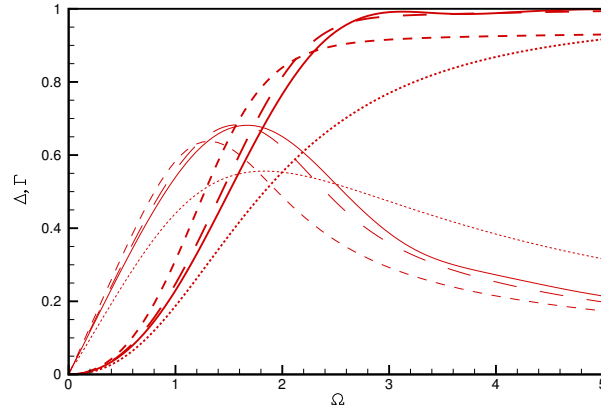
FIGURE 10. Real part Γ (thick) and Imaginary part Δ (thin) of the Rayleigh conductivity for a hole of zero thickness, for $Re = 100$ ($\cdots$), $Re = 500$ ($\cdot - \cdot$), $Re = 1500$ (— —). The plain lines (—) correspond to the Howe Model.

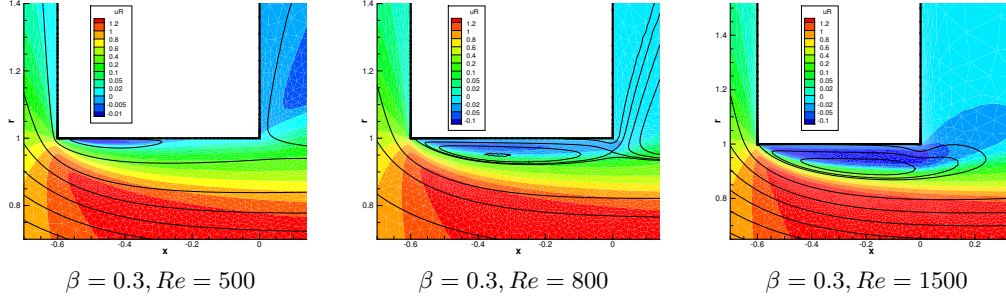$$\beta = 0.3, Re = 500 \qquad \beta = 0.3, Re = 800 \qquad \beta = 0.3, Re = 1500$$

FIGURE 11. Structure of the recirculation region. Colors levels : axial velocity. Black lines : streamfunction.
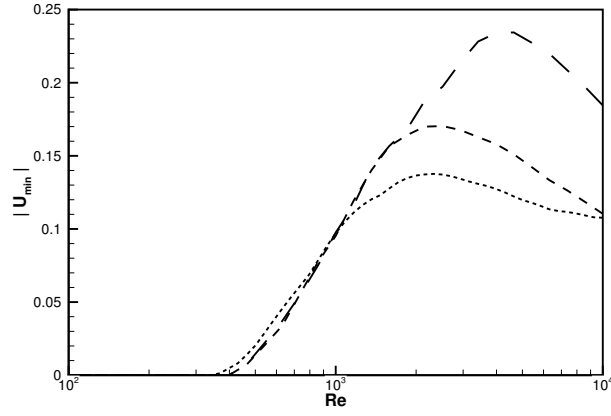
FIGURE 12. Intensity of the recirculation flow inside the hole as function of Re, for $H_h/D_h = 0.1$ (dots), $H_h/D_h = 0.3$ (dashes), $H_h/D_h = 1$ (long dashes).

5. The nonzero thickness case

5.1. *Steady base flows : study of the recirculation region*

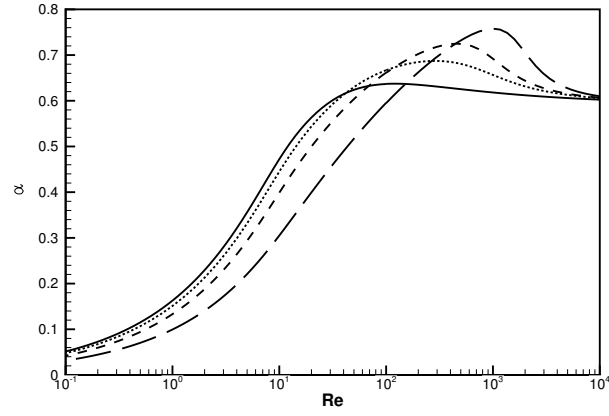*David Fabre, Paul Bonnefis, Paolo Luchini, and Flavio Giannetti*

FIGURE 13. Vena contracta coefficient as function of Re, for $H_h/D_h = 0$ (full line), $H_h/D_h = 0.1$ (dots), $H_h/D_h = 0.3$ (dashes), $H_h/D_h = 1$ (long dashes).
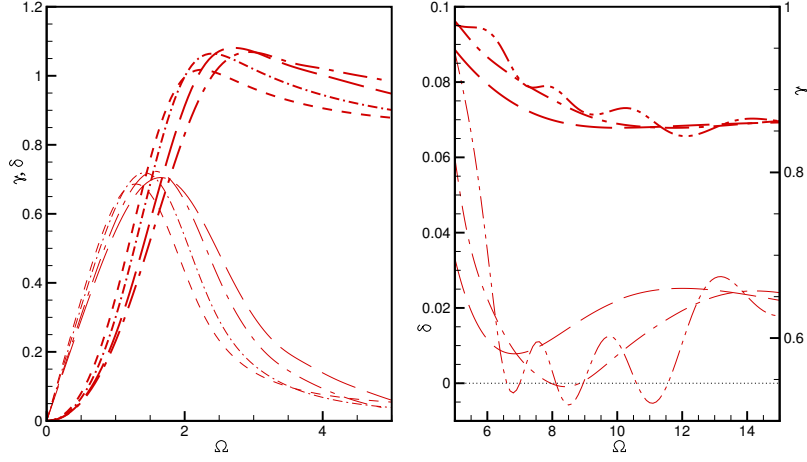
FIGURE 14. Real part Γ (thick) and Imaginary part Δ (thin) of the Rayleigh conductivity for a hole of thickness $\beta = 0.1$, for $Re = 100$ ($\cdots$), $Re = 500$ ($--$), $Re = 800$ ($\cdot - \cdot$), $Re = 1500$ (———), $Re = 3000$ (——). The right plot displays Δ in the range $5 < \Omega < 15$, with a magnified scale allowing to show the region where it becomes negative.
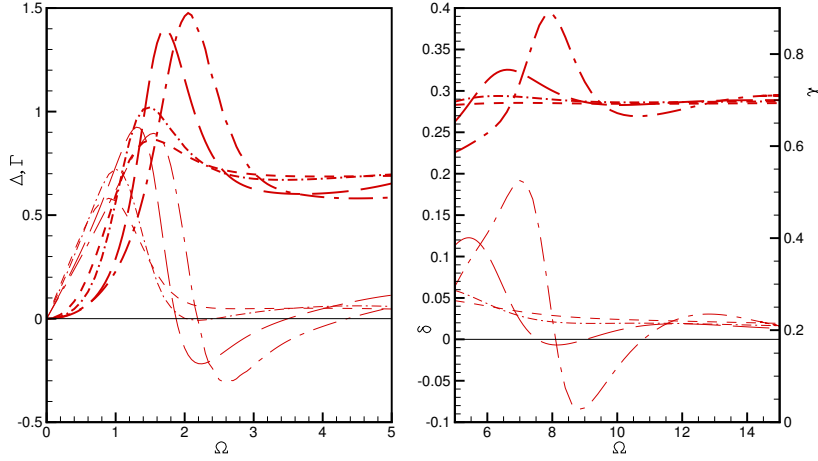

FIGURE 15. Real part Γ (thick) and Imaginary part Δ (thin) of the Rayleigh conductivity for a hole of thickness $\beta = 0.3$, for $Re = 100$ ($\cdots$), $Re = 500$ ($--$), $Re = 800$ ($- \cdot -$), $Re = 1200$ ($- \cdot \cdot -$), $Re = 1500$ (— —), $Re = 3000$ (— $\cdot$ —), $Re = 4500$ (— $\cdot \cdot$ —).

5.2. *Results : unsteady flow*

5.3. *Case of a rounded hole*

6. Global stability approach

Eigenvalue problem with homogeneous boundary conditions :

$$-i\omega[\hat{\mathbf{u}}; 0] = \mathcal{L}_0[\hat{\mathbf{u}}; \hat{p}]$$

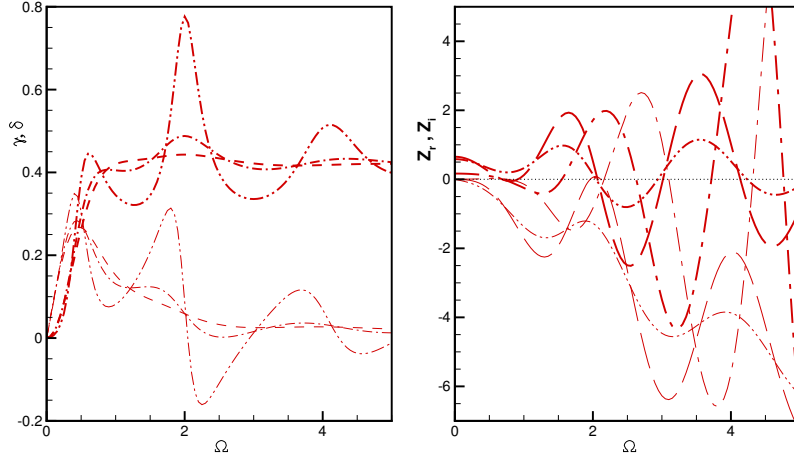$\hat{p} = 0$ at both inlet and outlet, but $\hat{q} \neq 0$.

FIGURE 16. Conductivity and impedance for a hole with thickness $\beta = 1$: (a) Real part Γ (thick) and Imaginary part Δ (thin) of the Rayleigh conductivity for $Re = 100$ ($\cdots$), $Re = 500$ ($--$), $Re = 800$ ($\cdot - \cdot$), $Re = 1200$ ($-\cdots-$). (b) Real (thick) and Imaginary (thin) parts of the Impedance for $Re = 1200$ ($-\cdots-$), $Re = 1500$ (———), $Re = 3000$ (——).

Link with the Conductivity : if $\Delta < 0$ then there is an eigenmode with $\omega_i > 0$ (to be demonstrated)

Illustration for $\beta = 0.3, Re = 800$ and $Re = 1500$.

SHOULD WE INCLUDE ALSO THE CASE OF A REACTIVE CAVITY ???

7. Conclusions

Appendix A. Numerical validations

Appendix B. The Rayleigh conductivity in absence of mean flow

FIGURES/SR_03_1500_1_33-eps-converted-to.pdf

(a) $\Omega = 1.33$

FIGURES/SR_03_1500_2_24-eps-converted-to.pdf

(b) $\Omega = 2.24$

FIGURES/SR_03_1500_5_41-eps-converted-to.pdf

(c) $\Omega = 1.33$

FIGURES/SR_03_1500_8_15-eps-converted-to.pdf
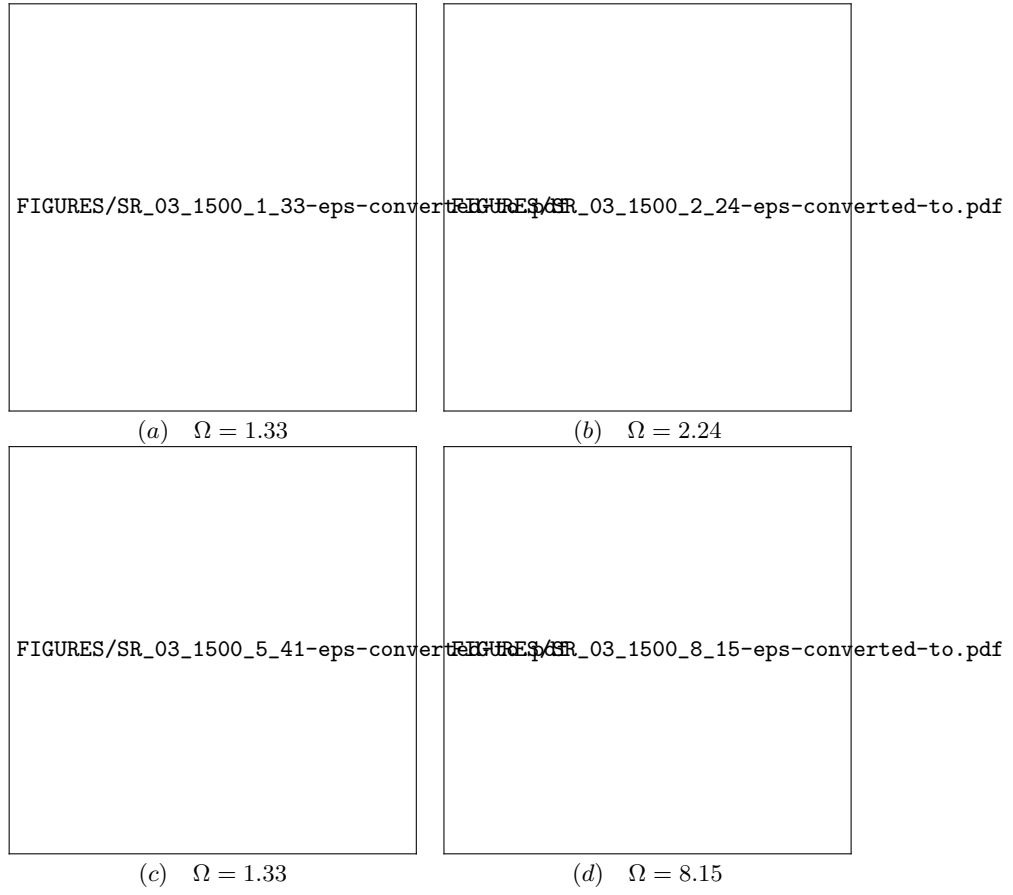
(d) $\Omega = 8.15$

FIGURE 17. Structure of the recirculation region. Colors levels : axial velocity. Black lines : streamfunction.